Tesi doctoral presentada per En/Na

Marc MANERA MIRET

amb el títol

"Cosmologia i Formació d'Estructures"

per a l'obtenció del títol de Doctor/a en

CIÈNCIES FÍSIQUES

Barcelona, 27 de juny del 2007.

Facultat de Física
Departament de Física Fonamental

UNIVERSITAT DE BARCELONA

Part III

Bias in Large Scale Structure

Chapter 14

Local halo biasing

Summary

After a theoretical introduction on clustering correlation functions and bias, I present reults for the local halo bias in the MICE intermediate simulation.

14.1 Motivation

In the new era of precision cosmology, simulations have emerged as a necessary step in our effort to understand structure formation in the universe. In fact they should be seen as the natural link between theory and observations. A link which may allow us to approach separately the different physical contributions that combine in an observation and also to understand better the systematics and statistical errors.

Part III of this thesis is devoted to study the local halo bias and the halo clustering by using a cosmological dark matter simulation, the MICE intermediate simulation. The main goal here is to test the validity of the local bias model. In this model, presented below, the bias is considered local and deterministic. In reality however, the bias is neither local (due to tidal forces) nor deterministic, but stochastic (see Dekel & Lahav 1999). We would like to address the question of to what extend the local bias can be applied to recover the predictions presented in chapter 2 for the growth of structure using statistical measurements as the variance, the skewness or the correlation functions. To do so, we will work with comoving data from the simulation at two different red shifts $z = 0$

and $z = 0.5$. By working with comoving data we concentrate on the gravitational evolution and structure formation and get rid of redshift distortions and other lightcone effects, which might not be directly related to the question addressed. Nevertheless, the inclusion of lightcone effects and redshifts distortions have to be considered as the natural next step in our study, since at the end we want to model the observational data.

14.2 Correlation functions and biasing

14.2.1 Two and three point correlation functions

The two and three-point correlation functions are defined, respectively, as (Bernardeau et. al. 2002)

$$\xi(r_{12}) = \langle \delta(r_1)\delta(r_2)\rangle \tag{14.1}$$

$$\zeta(r_{12}, r_{23}, r_{13}) = \langle \delta(r_1)\delta(r_2)\delta(r_3)\rangle \tag{14.2}$$

where $\delta(r)$ is the local density contrast at position r smoothed over a given characteristic R scale. The expectation value is taken over different realizations of the cosmological model. In practice, we apply the ergodic theorem and perform the average over different spatial positions in our universe, which are assumed to be a fair sample of possible realizations (Peebles 1980). As a particular case, when in the two or three points are in fact the same ($r_1 = r_2 = r_3$), we get the variance and the skewness. They are defined as

$$\sigma^2 = \langle \delta^2 \rangle = \frac{1}{N}\sum_{i=1}^{N} \delta_i^2 \tag{14.3}$$

$$m_3 = \langle \delta^3 \rangle = \frac{1}{N}\sum_{i=1}^{N} \delta_i^3 \tag{14.4}$$

where the sum (allowed due to the ergodic theorem) is over a fair sample of points in the simulation. In this case, one typically considers these quantities as a function of the smoothing radius R, while the correlation functions are displayed as a function of pair separation r_{12}. In the limit $r_{12} \gg R$ correlations are independent of R, while for $r_{12} \simeq R$ both measurements are closely related.

It is also convenient to define the normalized skewness and the hierarchical Q_3 parameter as follows (Growth & Peebles 1977)

$$S_3 = \frac{m_3}{\sigma_2^4} \tag{14.5}$$

$$Q_3 = \frac{\zeta(r_{12}, r_{23}, r_{13})}{\zeta_H(r_{12}, r_{23}, r_{13})} \tag{14.6}$$

$$\zeta_H \equiv \xi(r_{12})\xi(r_{23}) + \xi(\vec{r}_{12})\xi(r_{13}) + \xi(r_{23})\xi(r_{13}), \tag{14.7}$$

where we have introduced a definition for the "hierarchical" three-point function ζ_H. Based on early galaxy measurements of ζ, the Q_3 parameter was thought to be roughly constant as a function of triangle shape and scale (Peebles 1980), a result that is usually referred to as the hierarchical scaling. It was later shown (Fry 1984) that one expects deviations from this scaling due to gravitation clustering, which creates filamentary structure.

To describe the three parameters that define the ζ or Q_3 triangle , it has been customary to use the two sides of the triangle r_{12} and r_{23} (which are typically comparable in side) and the angle α between them:

$$cos(\alpha) = \frac{\vec{r}_{12}}{r_{12}}.\frac{\vec{r}_{23}}{r_{23}} \tag{14.8}$$

with $0 < \alpha < 180$ deg.

The Q_3 parameter has been measured in surveys (Feldman et. al. 2001; Gaztanaga et. al. 2005) and in simulations (Scoccimarro et al. 1999; Barriga & Gaztanaga 2002; Gaztanaga & Scoccimarro 2005). It shows a characteristic $U-shape$ (see figures 15.3 and 15.4) which results from gravitational instability: elongated triangles have larger probabilities because of the gravitational collapse. In the initial Gaussian field ζ, Q_3 and S_3 are all zero.

14.2.2 The local halo bias model

A simple model for halo or galaxy bias was introduced by Fry and Gaztañaga (1993). These authors assumed that the density contrast in the halos (or galaxy) distribution δ_h can be expressed as a general non-linear function of the local density contrast of dark matter, δ_m, so that: $\delta_h = F[\delta_m]$. On large enough scales, where the fluctuations in the density field are smoothed so that the matter

density contrast is of order unity or smaller, this relation can be expanded in a Taylor series

$$\delta_h = \sum_{k=0}^{\infty} \frac{b_k}{k!} \delta_m^k = b_1 \delta_m + \frac{b_2}{2} \delta_m^2 + \cdots \tag{14.9}$$

where the $k = 0$ term comes from the requirement that $< \delta_h >= 0$. Within this local bias model, at scales where $\xi_2 < 1$, we can write the biased (halo or galaxy) two and three point functions to the leading order in ξ (Fry & Gaztanaga 1993; Frieman & Gaztanaga 1994) as

$$\begin{aligned} \xi^h(r) &\simeq b_1^2 \, \xi(r) \\ Q_3^h &\simeq \frac{1}{b_1} \, (Q_3 + c_2) \end{aligned} \tag{14.10}$$

where $c_2 \equiv b_2/b_1$, and the $\simeq$ sign indicates that this is the leading order contribution in the expansion given by equation 14.9 above. We can also write the halo skewness as:

$$S_3^h = \frac{1}{b_1}(S_3 + 3c_2) \tag{14.11}$$

Thus, we can see that, in general, even when $\delta_m \ll 1$, the linear bias prescription is not accurate for higher-order moments, (i.e., Q_3), the reason being that nonlinearities in bias (i.e. c_2) generate non-Gaussianities of the same order as those of gravitational origin.

The linear bias term b_1 can produce distortions in the shape of Q_3, while the non-linear bias terms c_2 only shifts the curve. Because b_1 typically increases with the halo or cluster mass, the U-shape of Q_3 as a function of α is typically suppressed, resulting in a more hierarchical form of the 3-point function $\zeta \simeq \zeta_H$. Therefore, it is possible to use the shape of Q_3^h in simulations (or observations) to separate b_1 from c_2. This is done by comparing the dark matter predictions with the simulations (observations) data results and adjusting the bias parameters. This gives an estimate of the linear bias b_1 which is independent of the overall amplitude of clustering ξ. This approach has already been implemented for the skewness S_3 (Gaztañaga 1994, Gaztañaga & Frieman 1994), the bispectrum (Frieman & Gaztañaga 1994, Fry 1994, Feldman et al. 2001, Verde et al. 2002) or the angular 3-point function (Frieman & Gaztañaga 1999, Gaztañaga & Scoccimarro 20005, Gaztañaga et al. 2005).

14.2.3 Press-Schechter and Sheth-Tormen halo model predictions

In the spherical collapse model, expanding the conditional mass function for halos around the critical density contrast it is possible to find predictions for the bias on very large scales (Mo et al. 1997,Scoccimarro et al. 2001, Cooray & Sheth 2002)

$$\begin{aligned} b_1(m,z) &= 1+\epsilon_1+E_1 \\ b_2(m,z) &= 2(1+a_2)(\epsilon_1+E_1)+\epsilon_2+E_2 \quad a_2=-17/21 \end{aligned} \tag{14.12}$$

where the ϵ_1, E_1 and E_2 are defined in terms of the p and q variables as presented in section 3.2.

$$\begin{aligned} \epsilon_1 &= \frac{q\nu-1}{\delta_{sc}(z)} \qquad \epsilon_2=\frac{q\nu}{\delta_{sc}(z)}\left(\frac{(q\nu)^2-6q\nu+3}{\delta_{sc}(z)}\right) \\ E_1 &= \frac{2p/\delta_{sc}(z)}{1+(q\nu)^p} \qquad \frac{E_2}{E_1}=\frac{1+2p}{\delta_{sc}(z)}+2\epsilon_1 \end{aligned} \tag{14.13}$$

Again $\nu=\delta_{sc}(z)/\sigma_2(z)$ where δ_{sc} is the critical density contrast for collapse at a given redshift z, $\delta_{sc}(z)$. The Halo model predictions correspond to a fixed halo mass, $b_i(m)$, while we would like to have predictions for halos above a certain mass $b_i(m>M)$, which we will get from simulations. One could relate both estimations through the relation:

$$b_i(m>M)=\frac{1}{n_h}\int_{m>M} dm\ n(m)\ b_i(m), \tag{14.14}$$

where $n(m)$ is the halo mass function, which we can take to be that of Sheth and Tormen 2002 (ST) or the Press-Schechter one (PS). And the halo number density is given by

$$n_h=\int_{m>M} dm\ n(m) \tag{14.15}$$

The unconditional halo mass functions $n(m)$ have been given in section 3.2. Note that the Sheth and Tormen (ST) mass function have two free parameters p and q. They are usually taken to be $p\simeq 0.3$ and $q\simeq 0.75$, but other values of the parameters can fit as well the simulations. In this

chapter we will show predictions for both the former values and also for $q = 0.2$ and $p = 0.8$. This will give us an idea of how adjustable is the ST fit to the simulation. The Press-Schechter (PS) predictions correspond to the values of $p = 0$ and $q = 0.5$.

If one have a model for populating galaxies in halos, i.e a halo occupation distribution (HOD) that give the number of galaxies of a given type (i.e., luminosity and color) given the mass of the halo $< Ng|m >$, then we can introduce it in equations 14.14 14.15 and obtain the galaxy bias. If the bias model works, looking at the observed galaxies would allow us to fit the (usually two) HOD parameters. For an approach of how this can be done with SDSS survey (and also to see the b_i dependence on mass) see, for instance, Sefusatti & Scoccimarro (2005) .

14.3 The MICE intermediate simulation

We will analyse the halo bias and clustering from the MICE intermediate dark matter simulation [1]. This simulation have been run with Marenostrum at the Barcelona Supercomputer Center using the L-GADGET code, periodic boundary conditions, and 128 processors. Two hundred comoving outputs from $z = 1.4$ to $z = 0$ have been produced (12 TBytes of data). In this thesis we will use the $z = 0.0$ and the $z = 0.5$ outputs. They have $N = N_{1D}^3 = 1024^3$ dark matter particles over a cubical box of size $L = 1536 Mpc/h$. This particles have been put in cubic cells of 4Mpc/h producing a density mesh, from which we will compute the correlation functions and the direct local bias. The particle mass resolution of the simulation can be easily computed and it is

$$M = 27.75 \left(\frac{L}{N_{1D}}\right)^3 \Omega_m 10^{10} M_\odot/h \simeq 2.34\ 10^{11} M_\odot/h \tag{14.16}$$

The cosmological model parameters for the simulation are $\Omega_m = 0.25$, $\Omega_\Lambda = 0.75$, $\Omega_B = 0.044$, $n_s = 0.95$, $h = 0.7$ and $\sigma_8 = 0.8$. The softening length of the simulation is 50 Kpc/h.

A list of groups with 20 or more particles is provided on the fly by the Friends of Friends algorithm in the GADGET code. We have set the linking length to be 0.168 which results in 2729833 groups at z=0, and 2110669 groups at z=0.5. The central positions of all groups in the simulation have been located by P.Fosalba and we will use them for the computing the correlation function.

[1] For more information of the simulations we have run in the MICE collaboration team see http://segre.ieec.uab.es/fjc/LSS/MN/ and http://segre.ieec.uab.es/fjc/LSS/MN/download.

14.4 The Mass function

We have computed the cumulative mass function for halos in the simulation We show it in figure 14.1 for redshifts $z = 0$ (upper black curve) and $z = 0.5$ (lower black curve). Errors in the mass function are shown as the with of the curve and are computed by means of the Jack-knife method with 64 subsamples. For comparison we have also plotted the Press-Schechter (PS) prediction in red and the Sheth and Tormen (ST) prediction in blue. As expected the PS prediction produces more small mass halos and less high mass halos than the simulation. The Sheth and Tormen predictions are shown for $p = 0.2, q = 0.8$ and $p = 0.3$,$q = 0.75$. They fit much better the simulation measurement.

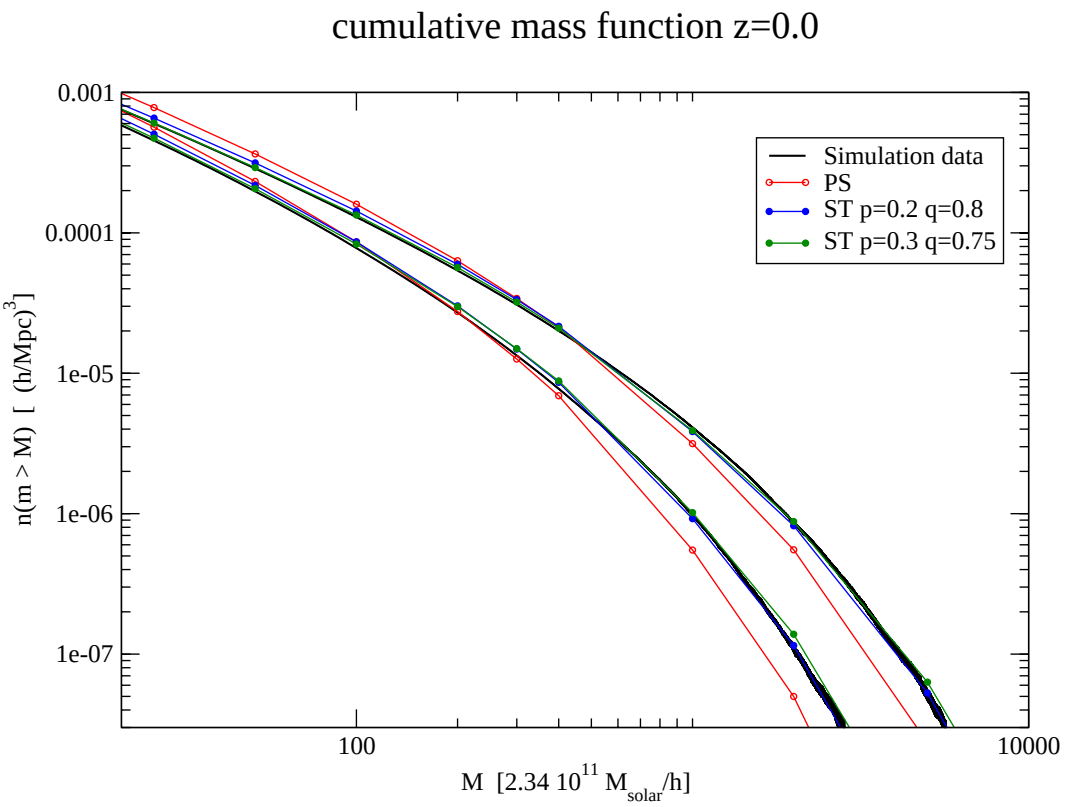

Figure 14.1: Cumulative mass function for halos in the MICE simulation at redshifts $z = 0$ (upper curves) and $z = 0.5$ lower curves. Compare them with PS predictions (orange) and the ST q=0.2 p=0.8 (blue) and p=0.3 q=0.75 (green) predictions

14.5 Measuring halo bias by direct δ_m δ_h comparison

In this chapter we are interested in determining the local bias parameters directly. In order to do so we will compare at different points the (smoothed) halo density contrast δ_h with the local (smoothed) matter density fluctuation δ_m. This will give an scatter plot of the relation $\delta_h = F[\delta_m]$, from which we can obtain b_1 and c_2 by means of a least mean square fit to the local bias parabola (equation 14.9). We have evaluated the $\delta_m - \delta_h$ relation at ~ 16000 points to fit the parameters, and have checked that increasing the number of points to ~ 110000 does not improve significatively the fit. Errors in the b_1 and c_2 parameters have been computed using the Jack-knife method with 64 subsamples.

One issue to be addressed is the dependence of the fit on the chosen smoothing scale. We have smoothed the mesh density field of the simulation with a Gaussian filter of radius R_s, which can vary. In figure 14.2 we show the scatter plots of halos of $M \geq 50 \times 2.34 \cdot 10^{11} M_{solar}$ for three different smoothing radius $R_s = 5, 10, 20 Mpc/h$ and for two redshifts, $z = 0$ and $z = 0.5$. We can see that for the smallest smoothing radius the scatter of points is very big. In this case there are even points with $\delta_m \geq 1$ which may situate us in a regime where the Taylor expansion of $F[\delta_m]$ can not be applied. When the radius is larger the scatter gets reduced and all points (except maybe a negligible number) will have $\delta_m < 1$. To get a better idea of the convergence of the fit we show in figures 14.3 and 14.4 the dependence of b_1 and c_2 on the smoothing radius for several halo minimum masses. The Jack-knife errors are also plotted. As expected, we see that the values of b_1 and c_2 change significatively as we increase the smoothing radius R_s from 5 to $20 - 25$ Mpc/h, from where they start to converge to their large scale values. Note also (figure 14.3) that the convergence seems slower for the higher mass halos and lower redshifts. In our study, to be conservative, we will take an smoothing radius of $30 Mpc/h$ as the one where the convergence regime has been reached. Scatter plots with their fitting curves for this smoothing radius are shown in figures 14.5 ($z = 0$ case) and 14.6 ($z = 0.5$). It is easy to see that, as the mass increases the curve changes its slope and also passes from slightly convex to concave form. This is the change in sign of c_2. With increasing mass the scatter also becomes more prominent. This is logical since, for a given over density region in the matter field, we are looking for rare objects (more massive halos) and shot noise dominates.

In figure 14.7 we show the b_1 and c_2 dependence on halo mass for both redshifts we are studying.

The results from the scatter relation fits have been plotted in black. We can compare them with the PS predictions (orange) and ST predictions for $p = 0.2, q = 0.8$ (blue) and $p = 0.3, q = 0.75$ (green). Like in the mass function plot it is immediately seen that PS fails completely to fit the measurements. The ST predictions do a much better job, although they not reproduce exactly the simulation results. In fact the values $p = 0.2, q = 0.75$ seems to fit better the $b_1(m)$ relation than the $p = 0.3, q = 0.75$ values, while for the $c_2(m)$ relation is the other way around. As expected the errors in the b_1 parameter are smaller than the ones of the second order coefficient b_2 and its related value c_2. We can see that both b_1 and c_2 increase with redshift and mass. Curiously enough the theory predicts a decrease of the parameter c_2, but for halo masses that are lower than the ones provided by the simulation, so we can not prove this characteristic feature. In the next chapter we will compare the clustered based values of b_1 and c_2 with the measured values of b_1 and c_2 that we presented here. This will allow us to study the accuracy of the halo bias model.

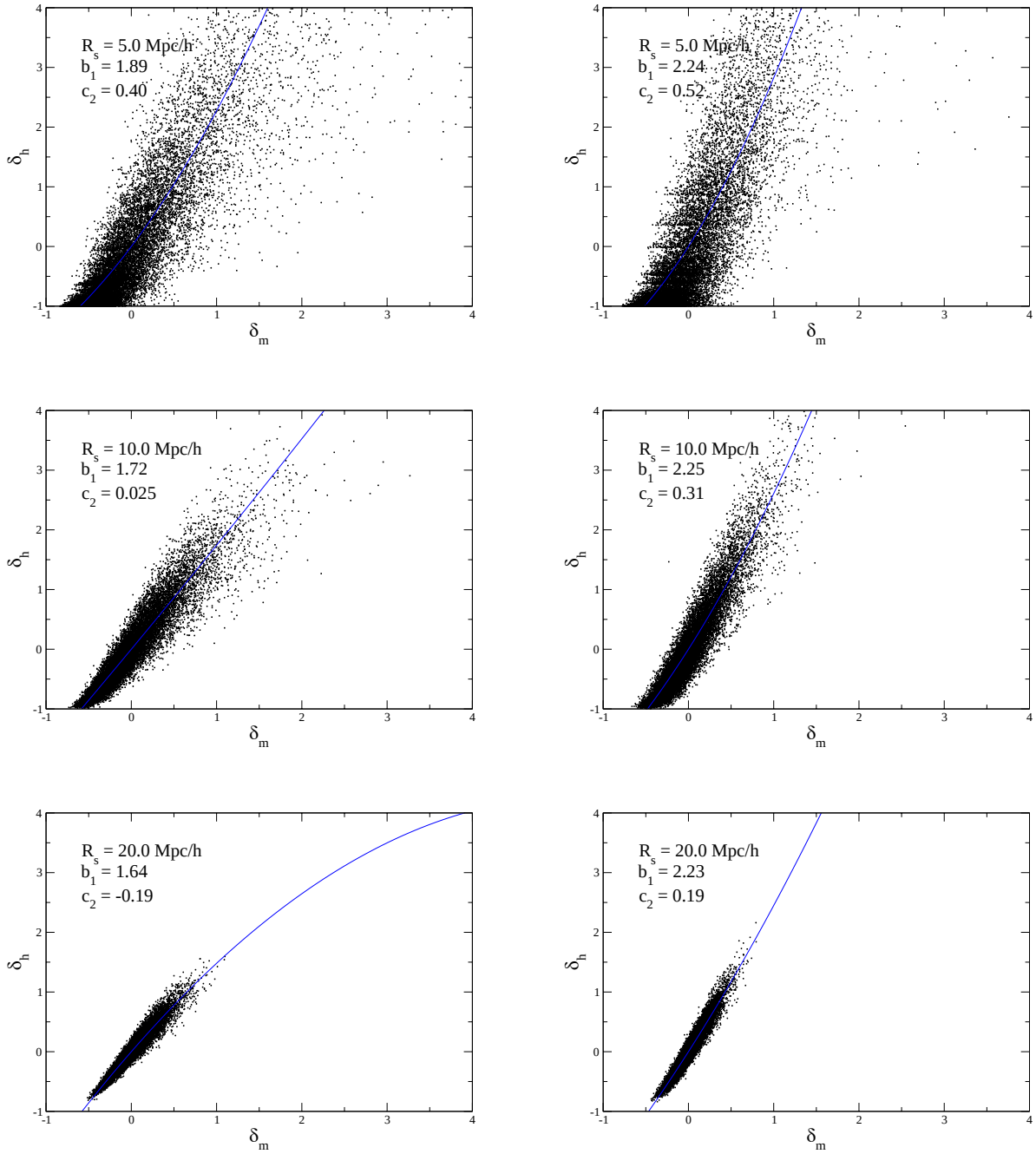

Figure 14.2: Scatter plots showing halo density contrast δ_h for halos of 50 or more particles versus dark matter density fluctuations δ_m. Results are shown for a different Gaussian smoothing as R_s as labeled in the figure. Left panels show results for the z=0 output of the simulation and right panels for z=0.5. In a continuous line we show the least square fit to the local bias parabola (equation 14.9)

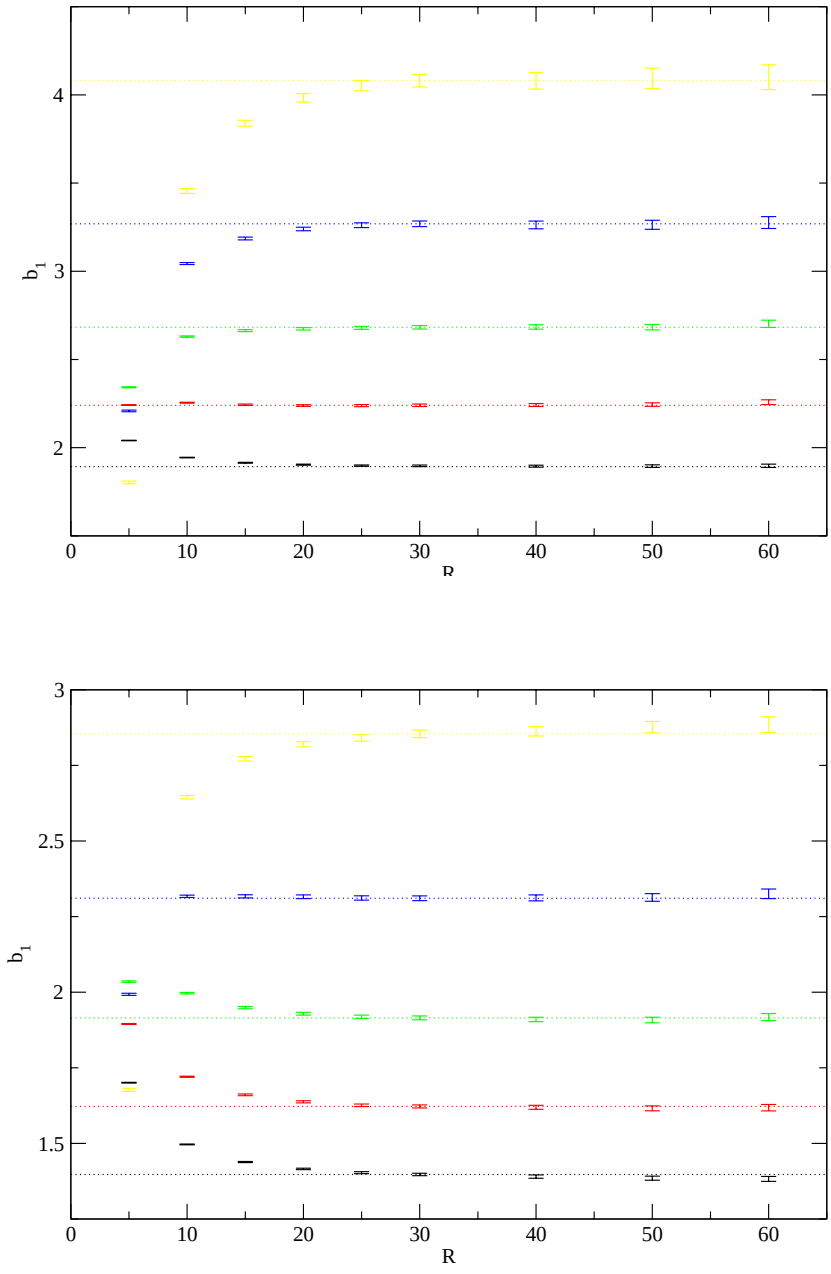

Figure 14.3: Dependence of b_1 on the Gaussian smoothing radius. Top panel corresponds to $z = 0.5$ and bottom panel to $z = 0$. Results are shown for different minimum number of particle per halo, n. In each panel from bottom to top n=25 (black), n=50 (red), n=100 (green), n=200 (blue) and n=400 (yellow). Dotted lines show the value at $R = 30Mpc/h$. The particle mass is $23.42 \times 10^{10} M_{solar}$

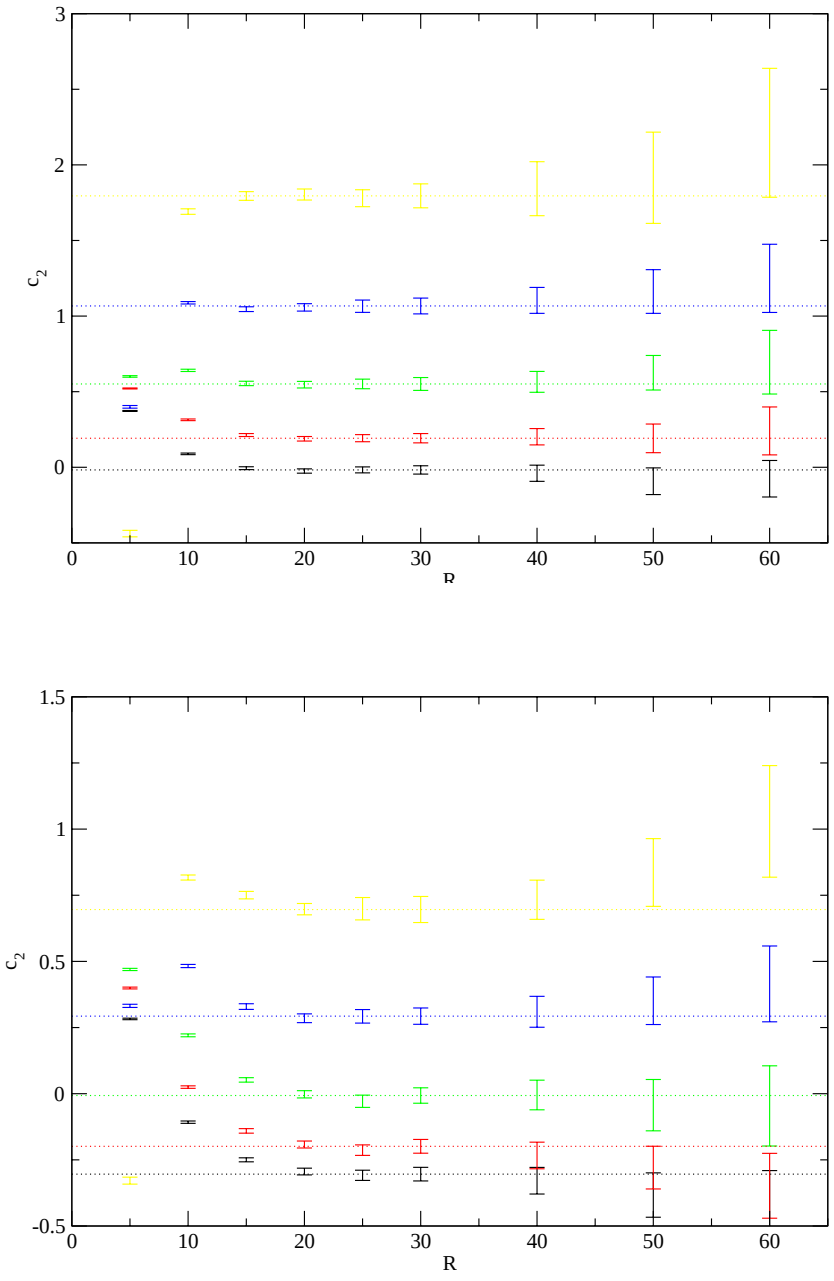

Figure 14.4: Dependence of c_2 on the Gaussian smoothing radius. Top panel corresponds to $z = 0.5$ and bottom panel to $z = 0$. Results are shown for different minimum number of particle per halo, n. In each panel from bottom to top n=25 (black), n=50 (red), n=100 (green), n=200 (blue) and n=400 (yellow). Dotted lines show the values at $R = 30Mpc/h$. The particle mass is $23.42 \times 10^{10} M_{solar}$

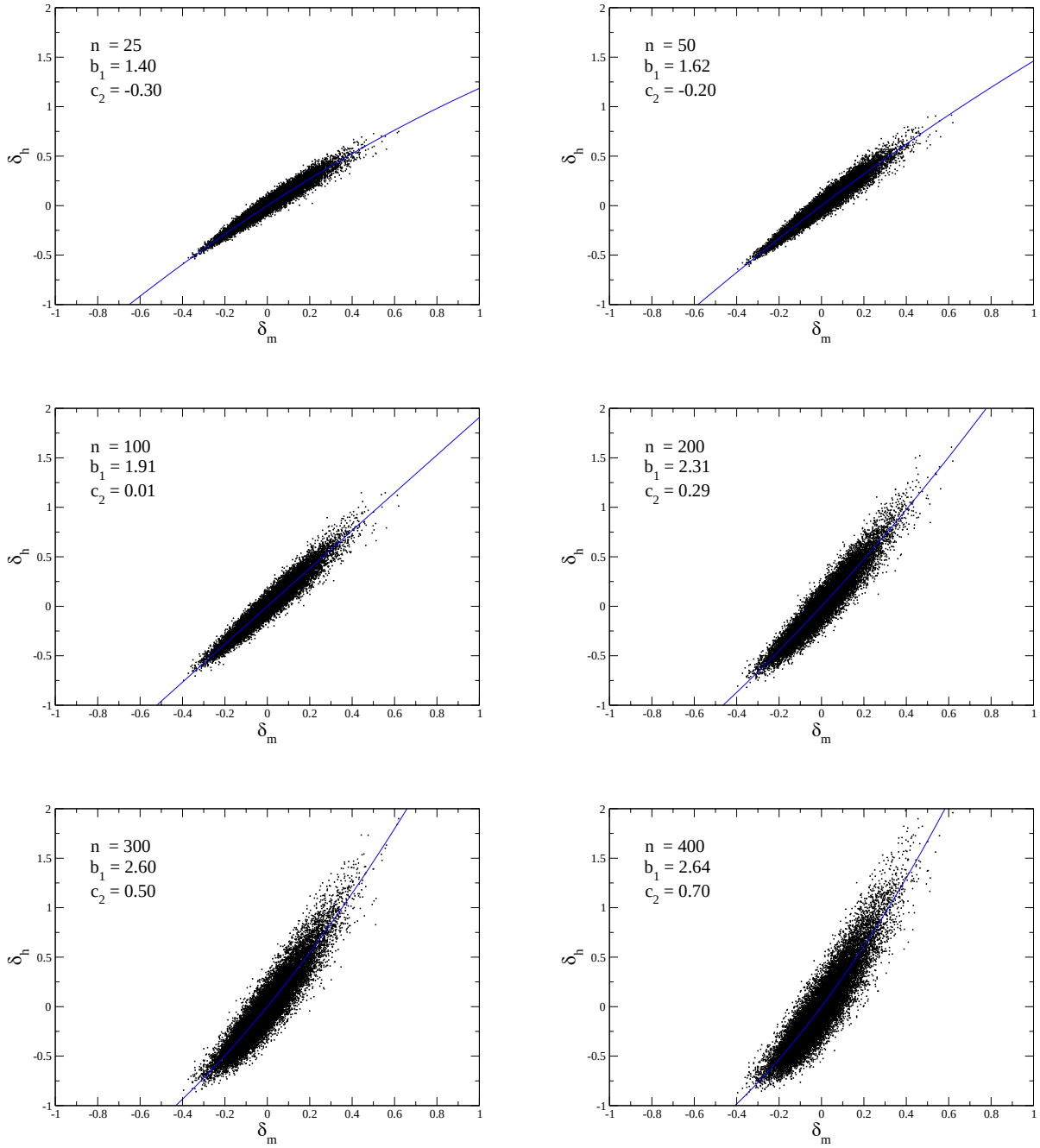

Figure 14.5: Scatter plots showing halo density contrast δ_h versus dark matter density fluctuations δ_m for a Gaussian smoothing with $R_s = 30$ Mpc/h. Results from MICE intermediate simulation at z=0. As labeled, different panels correspond to different minimum number of particles per halo. In a continuous line we show the least square fit to the local bias parabola (equation 14.9)

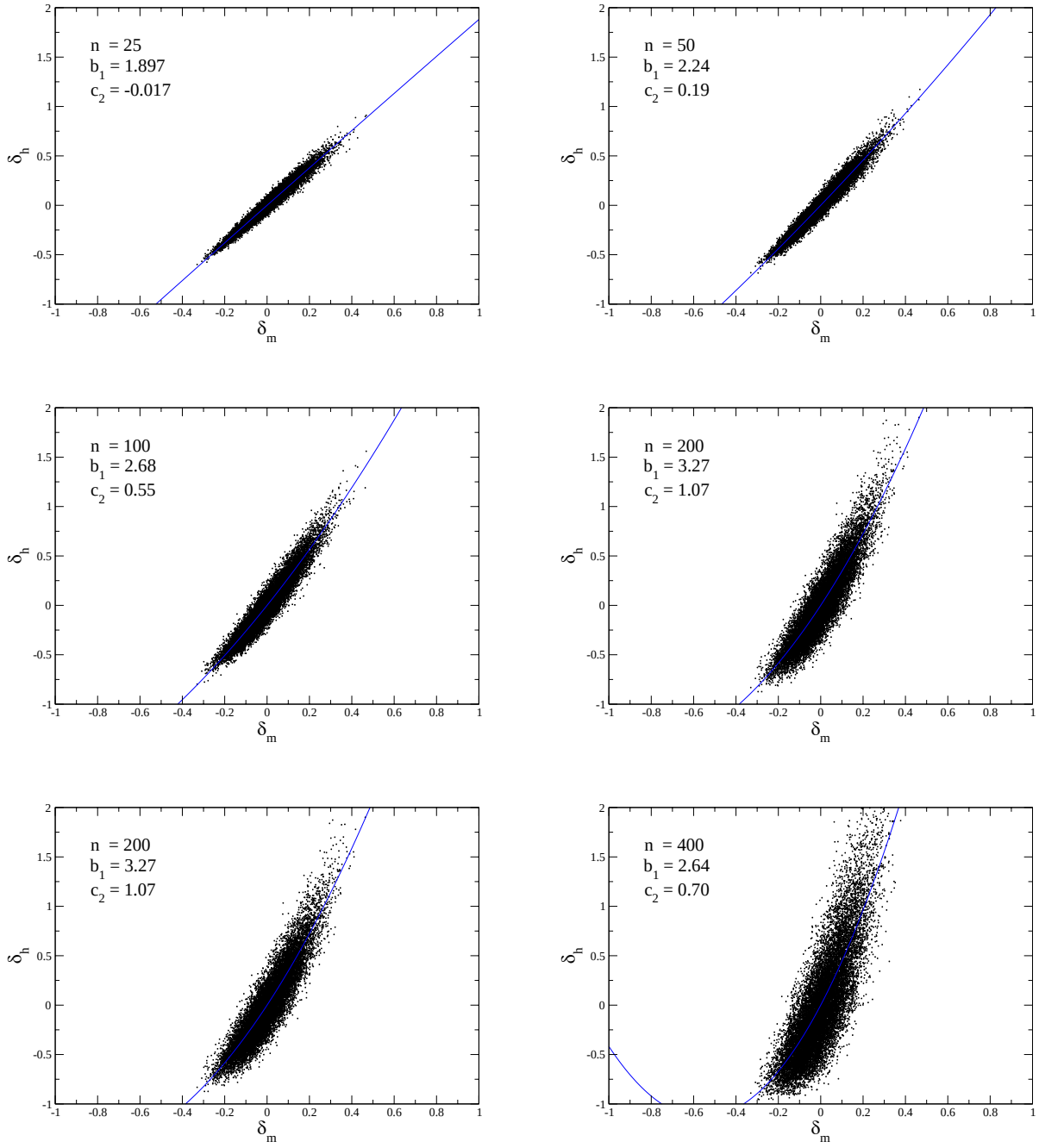

Figure 14.6: Scatter plots showing halo density contrast δ_h versus dark matter density fluctuations δ_m for a Gaussian smoothing with $R_s = 30$ Mpc/h. Results from MICE intermediate simulation at z=0.5. As labeled, different panels correspond to different minimum number of particles per halo. In a continuous line we show the least square fit to the local bias parabola (equation 14.9)

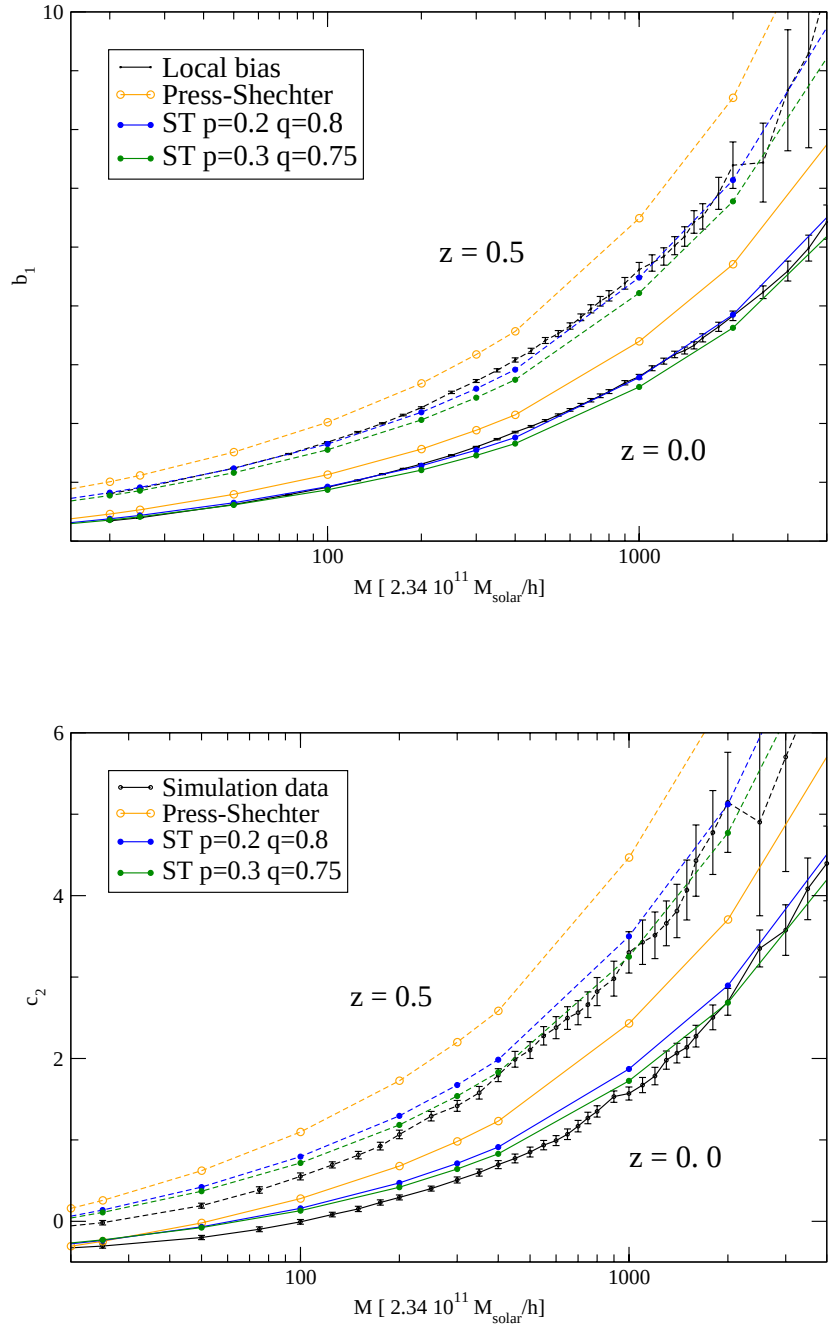

Figure 14.7: Dependence of b_1 (top panel) and c_2 (bottom panel) on the halos mass. In black we show the values measured directly from the δ_h-δ_m local relation in the simulation and compare them to the PS prediction (orange) and the ST prediction with p=0.2 q=0.80 (blue) and p=0.3 q=0.75 (green). As labeled in the figure each panel have both $z = 0$ and $z = 0.5$ results.

Chapter 15

Halo Clustering in Simulations

Summary

In this section I present the clustering of halos in the MICE intermediate simulation. Specifically we determine the bias parameters b_1 and c_2 from the halo variance and skewness and compare them to the local halo bias model. The two and three points correlation functions are also compared with the local bias model predictions.

15.1 The variance and the skewness

One of the most common ways of determining the linear bias of galaxies or halos is by comparing their variance with the measured/predicted matter variance. However, to perform the correct comparison one have to subtract the shot noise contribution. This contribution to the variance appears because galaxies and halos are not a continuous field, but a discrete one. For a top hat window function, $W_R(r) = \Theta(\mid r \mid - R)$ the shot noise is well known and it is equal to $1/n$ where n is the mean number of halos in a sphere of radius R. The shot noise corrected variance is therefore:

$$\sigma^2(R) =< \delta^2 > -\frac{1}{n} \tag{15.1}$$

where R stands for the window function smoothing scale. Not only the variance has to be shot noise corrected but also all the moments and cumulants of the halo field. The shot noise corrected

normalized skewness is found to be (Gaztanaga 1994):

$$S_3(R) = \frac{< \delta^3 > -3\sigma^2(R)/n - 1/n^2}{\sigma^2(R)} \tag{15.2}$$

where σ^2 is again the shotnoise corrected variance.

In this section we will compute the variance and the skewness by smoothing the halo density field in cubical cells of sides $L = 24Mpc/h$ and $L = 96Mpc/h$. The variance and the skewness obtained will be the equivalent to a top hat smoothing with $R = 14.9Mpc/h$ and $R = 59.5Mpc/h$ respectively. The shot noise correction can be taken as well as to be the same of an equivalent top hat smoothing (Baugh, Gaztanaga & Efstathiou 1995).

Regarding the dark matter in the simulation it is worth to notice that it is also a discrete field. Consequently, it will have its own shot noise correction, which will be obviously much smaller than the halo one, due to its higher number density. We have computed the variance and the skewness of the dark matter and see that they agree with the theoretical predictions. Note that when comparing the measured skewness to predictions one has to take into account the fact that we are smoothing the density field. For a top hat smoothing and CDM power spectrum the normalized skewness can be approximated by (Cooray & Sheth 2002; Bernardeau et. al. 2002)

$$S_3 = 4 + \frac{6}{7}\Omega_m^{-2/63} + \gamma_1 \tag{15.3}$$

where $\gamma_1 = \frac{dln(\sigma^2(R)}{dln(R))}$. Obviously for the Einstein-de-Sitter cosmology and no smoothing we recover the value $\frac{37}{4}$ given in section 2.2.

We now proceed to use the halos variance and skewness to compute the b_1 and c_2 as

$$b_1^2(R) = \frac{\sigma(R)}{\sigma_m(R)} \tag{15.4}$$

$$c_2 = (S_3^h\, b_1 - S_3^m)/3 \tag{15.5}$$

where R stands for the window function smoothing scale, and the subscripts h and m for halos and matter respectively. For computing c_2 we use the direct local b_1 as measured in the last chapter. The results are shown in figure 15.1. In the top panel we can see the linear local bias as computed

in the last chapter (black lines) compared to the linear bias deduced from the variance relation for different smoothing scales $R = 14.9$ (green points) and $R = 59.5$ (blue points). Errors for these points are computed by means of the Jack-knife method with 64 subsamples in the simulation. For clarity errors for the direct local bias determination (black lines) are not displayed, but can be picked out from the figures in the previous chapter. As expected from theory the larger the scale smoothing R is, the better the agreement with the local bias model. If the smoothing scale is small the density contrast could take large values and the Taylor expansion in equation 14.9 would not apply. We have also seen that the local bias starts to converge actually when the Gaussian smoothing radius is of the order of $25-30Mpc/h$ (that would correspond to a spherical top hat radius of about $50-65Mpc/h$). Therefore, knowing this, it is not surprising that at $z = 0$ and for $R = 14.9Mpc/h$ the bias from the variance comparison clearly fails to match the local bias. We can see a better agreement at z=0.5 which can be understood because the density fluctuations are smaller. In the top panel of fig 15.1 we have also plotted (as red points) the b_1 values obtained below from the two point correlation function. Note that these points fit the local bias model and, at the lower halo masses, they almost overlap the green and blue points (which might seem not to be plotted).

In the bottom panel of figure 15.1 we shown values of c_2 as a function of the halo mass for two different cubical cells with an equivalent spherical radius of $R = 14.9Mcp/h$ (green points) and $R = 59.5Mpc/h$ (blue dots). Errors are given by means of the Jack-knife method with 64 subsamples. These values obtained from the skewness can be compared with the local c_2 values obtained from δ_m-δ_h direct relation (black line). In this case errors are not plotted for clarity but can be picked out from the corresponding figures in the previous chapter. As in the b_1 panel we see that the $R = 14.9Mpc/h$ smoothing radius is still too small to fit the large scale local bias values, which are in contrast well matched by the $R = 59.5Mpc/h$ results.

15.2 Two point correlation function

We have computed the two point correlation function $\xi_2(r)$ for the matter and halo density contrast in the simulation. To estimate $\xi_2(r)$ we have used the 4Mpc/h density mesh of the simulation and average all the mesh points separated by $(r \pm \Delta r)$, where $\Delta r = 0.5Mpc/h$. The results for the matter correlation function and for different halo masses (given by the minimum number of particles

per halo) are shown in figure 15.2. The top panel shows the $z = 0$ case and the bottom panel the $z = 0.5$.

As expected the more massive the halos the more biased the correlation function. Note as well what is called the stable clustering, i.e., the fact that for a given halo mass threshold the absolute value of ξ_2 remains approximately constant in redshift while the matter correlation function decreases (in redshift). This could be understood however because halos of a given mass threshold but at different redshift do not correspond to the same Lagrangian mass. The ones at higher redshift are situated in a rarer (less expected) matter fluctuations, being therefore more biased.

The measured correlation function from the simulation shows very clearly the acoustic peak at about $\sim 110 Mpc/h$ for both the matter and the halo functions. This can be seen in the figure 15.2. For comparison, in this figure we have also plotted the Linear Perturbation Theory (PT) prediction and the Renormalized Perturbation Theory (RPT) prediction for the correlation function, which has been kindly provided by M. Crocce. In the Standard Perturbation Theory PT one expands the equation of motion around their linear solution, assuming that fluctuations are small. The power spectrum can be split into a linear part and higher order correlations. However, for scales approaching the nonlinear regime the truncation at any finite order in PT is not meaningful because neglected higher order contributions are important. The Renormalized Perturbation Theory (Crocce & Scoccimarro 2006; Crocce & Scoccimarro 2006b) gets around this limitation by making a resummation of an infinite subset of the contributions to the PT expansion. The RPT shows deviations of the linear theory at much larger scales that have been previously thought and already in the acoustic peak scale one gets a contribution of the nonlinear effects. (Crocce & Scoccimarro 2006). As can be seen in the figure these nonlinear contributions results into a smoother prediction for the acoustic peak shape in the RPT than in the standard PT. This seems to be actually in a better agreement with what we find in the simulations.

In this section we are basically interested in measuring the linear bias by comparing the 2-point matter and halo correlation functions. We will then compare these results with the local direct bias determination. For a given lower halo mass threshold we find the bias as

$$b(r) = \sqrt{\frac{\xi_2^h(r)}{\xi_2^m(r)}} \tag{15.6}$$

This bias, which is expected to be a constant in the local halo model ($b(r,m) = b_1(m)$), actually varies at different r due to cosmic variance. This variation gets more pronounced for larger scales (where we have few modes in the simulation) and for larger halo mass thresholds (since the number for statistics get reduced). We choose to determine $b_1(m)$ by averaging the bias at five points with $r = 10, 25, 35, 45, 55 Mpc/h$, where the cosmic variance is lower. From the dispersion of their values we will also get an error for b_1. Results are shown in red in the top panel of figure 15.1. We can see that, within its errors, they are roughly in accordance with the local bias determined directly from the δ_h-δ_m relation. The agreement is better for smaller halos and the prediction seems to be systematically above the measurements (but within errors) for the larger halos.

15.3 Three point correlation functions

We have computed the hierarchical relation $Q_3(\alpha)$ (see equation 14.8) for dark matter and halos in the simulation. We have used $r_{23} = 2r_{12} = 24 Mpc/h$ and r_{13} is given by the angle α. Results for $z = 0$ and $z = 0.5$ are shown respectively in figures 15.3 and 15.4. Each figure have four panels which correspond (clockwise from the top left panel) to four different minimum halo masses $M \geq 25, 123, 225, 325 \times [2.34 \cdot 10^{10} M_{solar}]$. Dark matter measurements are shown as blue triangles while halo measurements are in black circles. Errors are from the Jack-knife method and, for clarity, we only show them in the matter measurements. Errors in halos are at least as large as in the matter case. Notice the characteristic U shape of the hierarchical relation. It is an indication of the dark matter and halo large scale filamentary structure, i.e, aligned structures ($\alpha \sim 0$, $\alpha \sim 180 deg$) are more likely to be found that other configurations (for instance, equilateral triangles).

In figures 15.3 and 15.4 we have plotted the standard perturbation theory prediction for Q_3 as a dotted line. It is worth to notice that it matches very well the simulation results. This is, by using the b_1 and c_2 values obtained from the δ_m-δ_h direct fit, we make a prediction for the halo Q_3 at different masses, which is plotted as a red dashed line. Note that, as it is predicted in the halo bias model (see equation 14.10), the halo hierarchical relation compared to the matter one gets flattened (due to b_1) and shifted (due to c_2). This can be clearly seen, for instance, in the case of halos with 25 or more dark matter particles. At both redshifts, as predicted by theory, the measured matter Q_3 is almost the same. At redshift $z = 0.5$ we have a c_2 close to zero while at $z = 0$ its value is

$c_2 = -0.3$. This translate in a larger shift between matter and halos at $z = 0.5$ than at $z = 0$. We can also see that the Q_3 value at $\alpha = 0$ is lower at $z = 0.5$ than at $z = 0$. This is obviously due to its higher b_1 value. The agreement between simulation measurements for halos (black circles) and the predictions (red dashed lines) extends to the other halo masses. Consequently the results show a clear validation of the halo bias model

15.4 Conclusions: Does the local bias work?

In part three of this thesis we have used the MICE intermediate cosmological dark matter simulation to study the halo clustering and bias. We have seen that for a large scale smoothing of the halo density field (tipically a top hat radius $\sim 60Mpc/h$) the shot noise corrected variance and skewness are in agreement with (i.e., could reproduce) the local bias parameters b_1 and c_2 measured directly from the $\delta_m - \delta_h$ scatter relation in the simulation. At smaller smoothing scales ($R \sim 15Mpc/h$) the fluctuations are not yet small enough to converge to the bias model. We have also shown that the bias parameters b_1 and c_2, predict well, within sampling errors, the halo two point correlation function ξ_2 and the hierarchical Q_3 function for different halo masses. This should be understood as a validation of the local bias model power in modeling the large scale structure formation. Nevertheless, note that there seem to be some systematic differences for the larger halos.

15.5 Future steps: clustering in the lightcone

So far we have been looking at the clustering and bias of two comoving outputs of the MICE intermediate simulation. This have been very useful for studying the local bias model and the evolution of the structure. However, it is very important to keep in mind that, because the speed of the light is finite, observations do not come in as a comoving output. Our real observations are in fact in a lightcone, i.e, every object is seen at such time that the light that was emitted then has just now reached us. We are therefore very interested in having a simulation in a lightcone format, which will be extremely useful for comparing theory with observations. That's the next natural step to make.

Using the 200 comoving outputs of the MICE intermediate simulation we have already con-

structed a lightcone for the matter particles up to redshift $z = 1.4$. This lightcone covers a quarter of the sky and is large enough to encompass the survey geometry and depth of the upcoming Dark Energy Survey [1](DES). The next step would be to find the halos in the lightcone simulation. With them one could keep on studying the clustering of the large scale structure, and progress towards understanding our beautiful universe.

[1] http://darkenergysurvey.org

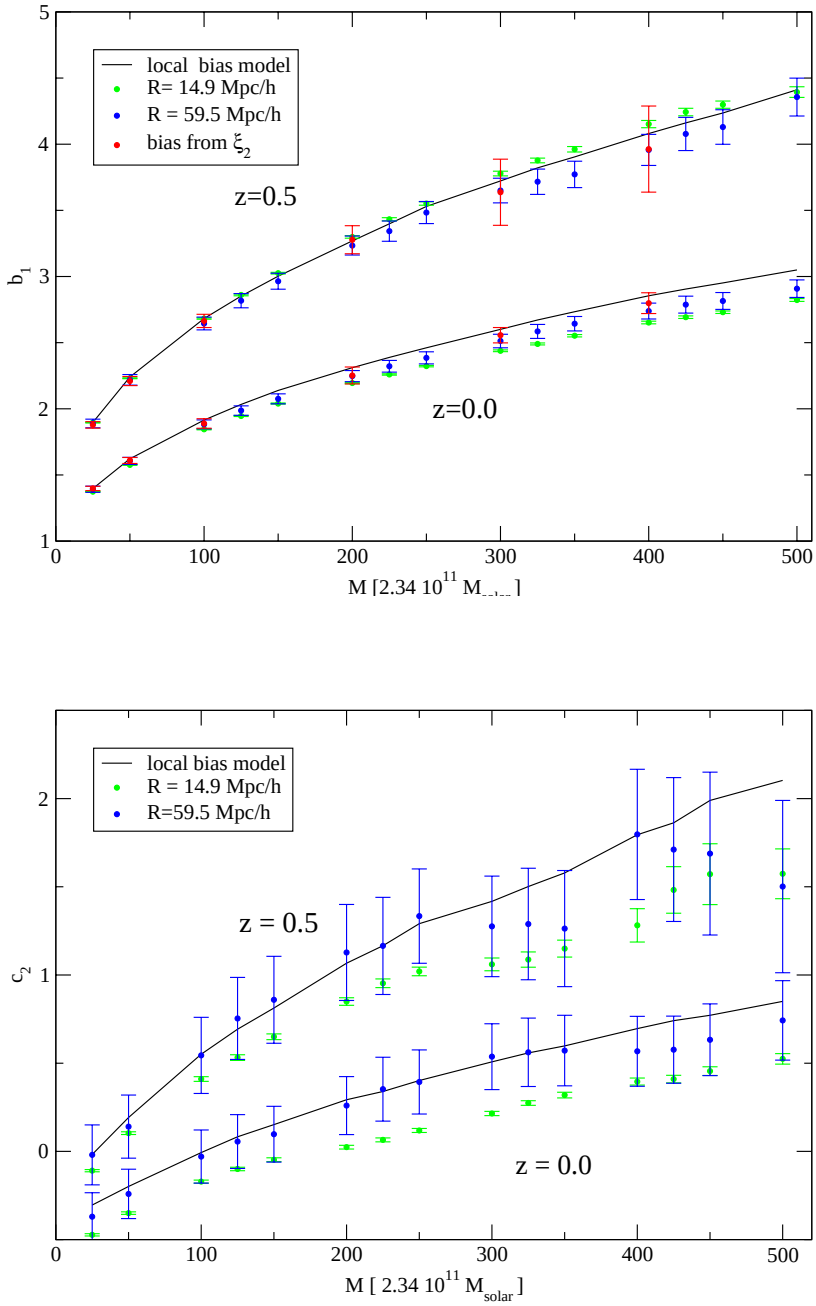

Figure 15.1: Dependence of b_1 (top panel) and c_2 (bottom panel) on the halos mass. Comparison of the b_1 and c_2 values as measured directly from the δ_h-δ_m local relation in the simulation (black lines) with the values obtained from the variance and normalized skewness for different smoothing radius (blue and green dots). In the top panel there is also plotted in red the linear bias b_1 derived from the two point correlation function. As labeled in the figure each panel have both $z = 0$ and $z = 0.5$ results.

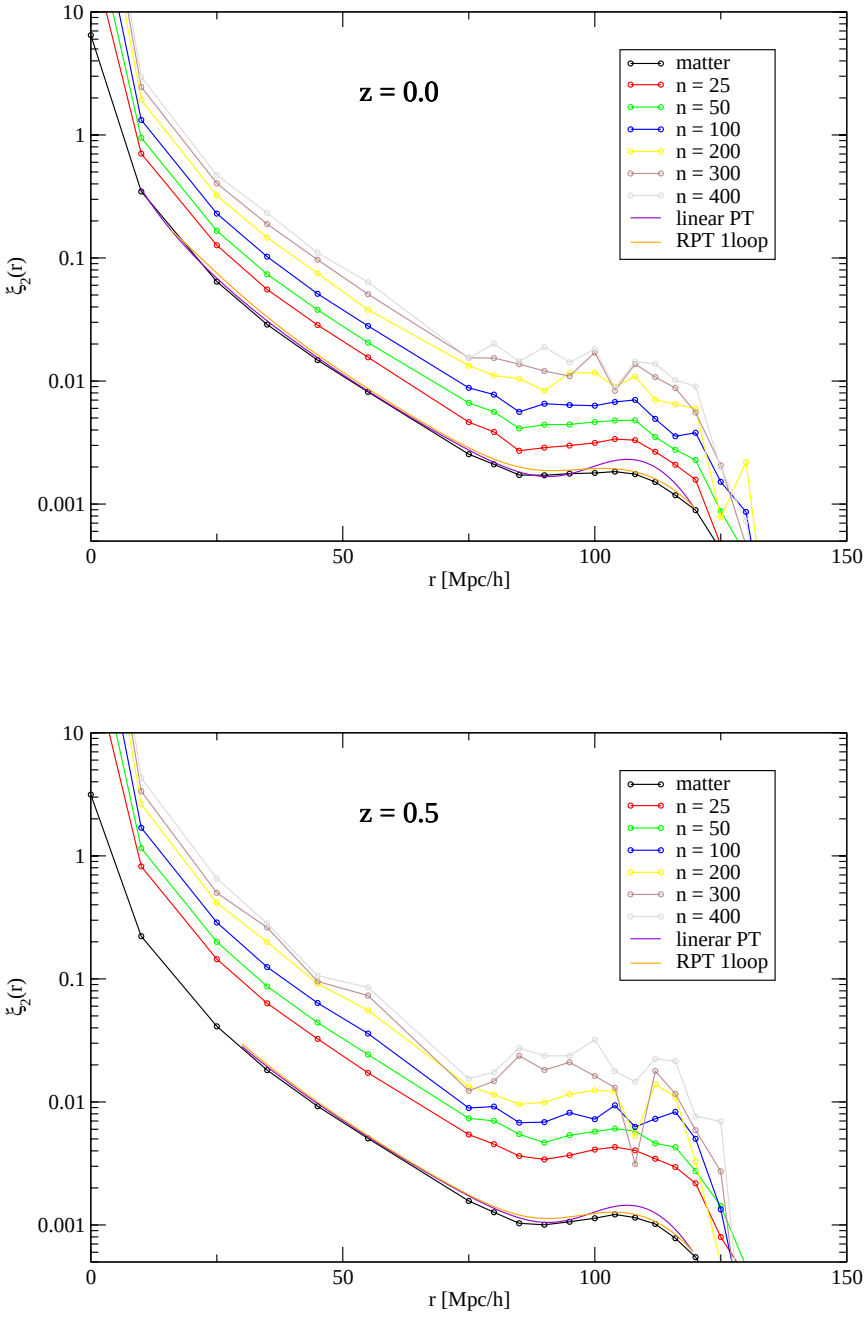

Figure 15.2: Two point correlation function $\xi_2(r)$ for different minimum number of particles per halo as labeled in the figure. The mass particle resolution is $M = 23.42 \cdot 10^{10} M_{solar}$. Top panel shows results for $z = 0$ and bottom panel for $z = 0.5$. For comparison we have plot also the RPT prediction and the linear PT prediction.

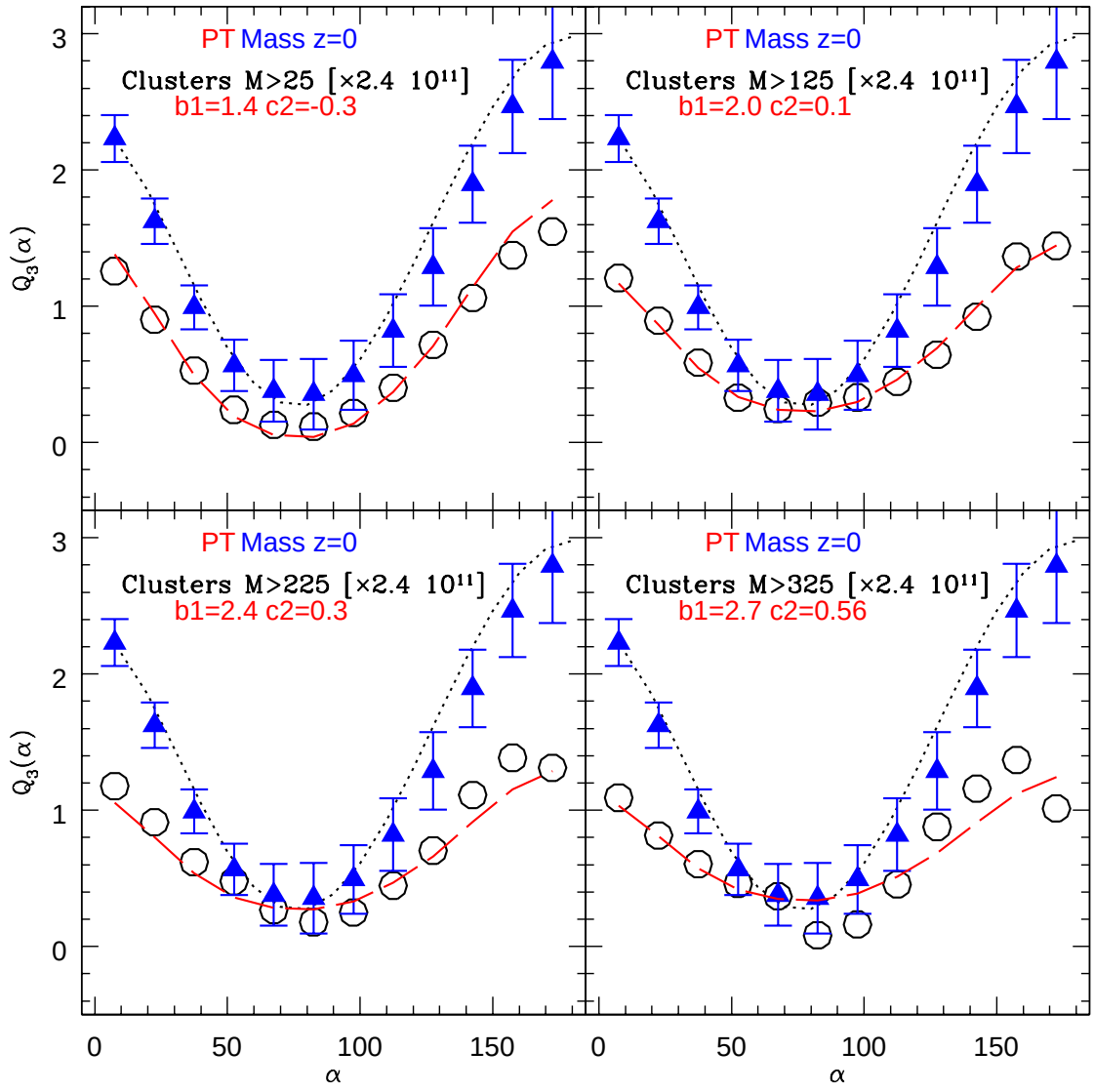

Figure 15.3: Hierarchical relation Q_3 for dark matter in the simulation (blue triangles) with $r_{23} = 2r_{12} = 24Mpc/h$ as compared to Q_3 in halos (black circles) of different masses: n = 25,125,225,325 clockwise from the top left panel. Black dotted lines show the matter prediction. Long dashed red lines show the biasing predictions (equation 14.10) for the values of b_1 and c_2 obtained directly from the δ_m-δ_h fit. Results shown at z=0.0

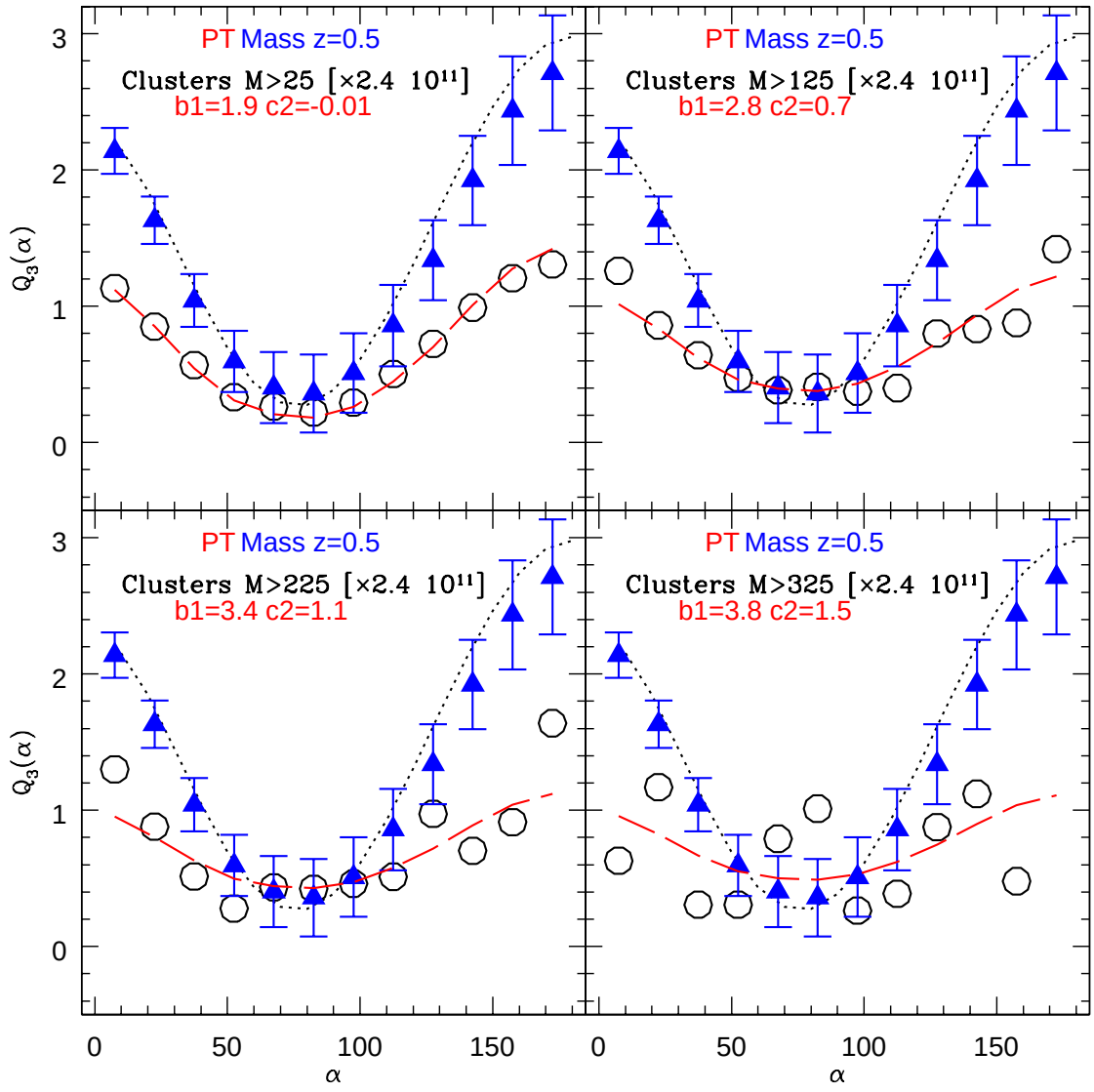

Figure 15.4: Hierarchical relation Q_3 for dark matter in the simulation (blue triangles) with $r_{23} = 2r_{12} = 24Mpc/h$ as compared to Q_3 in halos (black circles) of different masses: n = 25,125,225,325 clockwise from the top left panel. Black dotted lines show the matter prediction. Long dashed red lines show the biasing predictions (equation 14.10) for the values of b_1 and c_2 obtained directly from the δ_m-δ_h fit. Results shown at z=0.5

Chapter 16

Conclusions

This thesis has been a great adventure to progress in our understanding of the universe by means of studying the structure formation. It have been always in my mind to have an open approach that could somehow embrace both theory and observations, for when they are confronted is when science advances the most. Below, I summarise the main achievements and conclusions of this thesis:

- We have shown that structure formation can be successfully used to discriminate between different cosmological models and constrain their free parameters. This is complementary to other cosmological probes like the CMB temperature maps or the type Ia supernovae observations.

- We have introduced a formalism to compute the growth of dark matter perturbations in non-standard cosmologies. This formalism is obtained by rewriting the 4D Raychaudhuri's equation within the frame of the spherical collapse model. In this case the evolution of the density contrast is given only by the Friedmann equation and its derivative, which is meant to be obtained from the continuity equation. Thus, when having a Friedmann and continuity equation, this formalism provides a useful approximate solution for the growth of structure, without concerning us with Einstein's equations or (if known) the fully perturbative equations of the non-standard model.

- We have shown that the linear growth of both the Modified Polytropic Cardassian (MPC) model and the Dvali Gabadadze and Porrati (DGP) model is generally inhibited. Its suppression can be as much as 50% of the EdS case. The Generalized Chaplygin gas (understood as

dark energy) is however a completely different case. Its linear growth is extremely sensitive to the model parameters, so much that only the case which will pass an observational test is when we actually recover the ΛCDM cosmology. We have also computed the skewness of all three models, the differences to the standard value are of few percent (at most 10% for the extremely MPC cases), which is still out of the observational precision.

- We have shown that, at $z = 1.5$ the DGP and the MPC predict 2 and 4 times more clusters than the $\Lambda CDM model$. For the quintessence model we have found that the coupling of dark matter to dark energy tends to decrease the cluster number counts while the dark energy clustering produces the inverse effect. We have also shown that oscillations in the cluster number counts are a characteristic signature of the quintessence coupled models and they could probably be discriminated with the upcoming large scale structure surveys.

- We have compiled the ISW detections that several groups have performed by cross-correlating CMB-temperature maps with galaxies or other dark matter large scale structure tracers. We use the redshift dependence of the signal to constrain the growth of structure and give new evidence for dark energy, being the probability of a false detection only 3×10^{-5}. We have shown that the ISW signal can give complementary results to supernovae type Ia when constraining the (Ω_Λ, w) plane. For a flat cosmology the joint fit gives $\Omega_\Lambda = 0.70\pm0.05$ and $w = -1.02\pm0.17$.

- We have presented a new theoretical method to compute errors in the cross-correlation of sky maps in configuration space to constrain the ISW detections. This method (TC) has been shown to agree with the Monte Carlo errors computed from 1000 simulations of two cross-correlated sky maps, but it is faster to implement. It is also faster than the Jack-knife method (JK) which has the advantage of not assuming Gaussian statistics. The TC method takes into account the survey geometry, and consequently estimates well the error at big angular scales, where other methods like the theoretical harmonic space (TH) fails. The geometry in this method is encoded in two functions, for which we have provided analytical expressions that will give accurate results in most compact surveys. Despite their conceptual differences, for a realistic ΛCDM cosmology and a survey of 10% of the sky (like the SDSS or DES), when the covariance matrices are evaluated (only) up to 20 degrees, all four methods mentioned above have been shown to give almost identical constraints to the cosmological parameters.

- Finally, we have used the MICE intermediate cosmological dark matter simulation to study the halo clustering and bias. We have seen that, for a large scale smoothing of the halo density field, the shot noise corrected variance and skewness are roughly in agreement with the local bias parameters b_1 and c_2 measured directly from the $\delta_m - \delta_h$ scatter relation in the simulation. At smaller smooting scales (top hat radius $R \sim 15 Mpc/h$ instead of $R \sim 60.0 Mpc/h$) the fluctuations are not yet small enough to converge to the bias model. We have also shown that the bias parameters b_1 and c_2, predict well, within sampling errors, the halo two point correlation function ξ_2 and the hierarchical Q_3 function for different halo masses. This should be understood as a validation of the local bias model to relate the theory of the large scale structure with observations.